Letters

Fractional-Order Virtual Synchronous Generator

Yun Yu, *Graduate Student Member, IEEE*, Yajuan Guan, *Member, IEEE*, Wenfa Kang, *Student Member, IEEE*, Sanjay K. Chaudhary, *Senior Member, IEEE*, Juan C. Vasquez, *Senior Member, IEEE*, and Josep M. Guerrero, *Fellow, IEEE*

***Abstract*—In this letter, a novel control scheme is proposed by combining the fractional-order control and the virtual synchronous generator, whereby more degrees of freedom are involved in the controller design. A well-damped power control without oscillations is achieved. At the same time, a significant improvement in the inertial effect is attained. Both theoretical and experimental results have validated the feasibility.**

***Index Terms*—Fractional-order control (FOC), virtual synchronous generator (VSG), voltage-source inverter (VSI).**

I. Introduction

THE virtual synchronous generator (VSG) has been extensively used in various energy conversion applications. Its embedded inertia emulation plays an important role in limiting the rate of change of frequency (RoCoF) and maintaining the frequency stability of power-electronic-based systems. On the other hand, it often exhibits insufficient damping effects, which in turn may lead to poorly damped power oscillations [1].

Massive investigations have been conducted on its damping effect improvement. For example, the active-damping solutions using phase-locked loops (PLLs) were studied in [2] and [3]. Despite their effectiveness, the potential instability caused by the PLL could be problematic in the practical implementation. To avoid the PLL-related instability, the damping effect correction methods that adopt the power control law modification were investigated in [4], [5], [6], [7], and [8]. Specifically, the active-damping solutions that link the excitation and the angular frequency generation were proposed in [4] and [5]. Additional damping effects were realized in [6] by adding extra feedback of the angular frequency or its derivative term. The virtual impedance concept was adopted in [7] for damping purposes as well. Moreover, on the basis of the state feedback control, the active-damping strategy with a full state feedback was studied in [8]. Through an appropriate design of the feedback filters proposed in these works, the damping effect can be improved to some extent; however, the inertial response could be degraded at the same time [9], [10]. This inevitably affects the frequency dynamics under power perturbations, especially the RoCoF.

To avoid the inertial effect degradation, control schemes simultaneously considering the damping and the inertial effect were developed in [11], [12], and [13]. Specifically, Meng et al. gave a solution using the active power derivative in [11]. Solving the same problem, Rathnayake et al. developed a generalized VSG control scheme to avoid using the active power derivative filter in [12]. Unfortunately, using these control schemes, the improvements made in the inertial effect may not be enough to limit the RoCoF significantly. This shortcoming is here rectified by the fractional-order VSG (FOVSG). With the extended degrees of freedom introduced by the fractional-order control (FOC), a further improvement of the inertial response is achieved, along with well-damped power control.

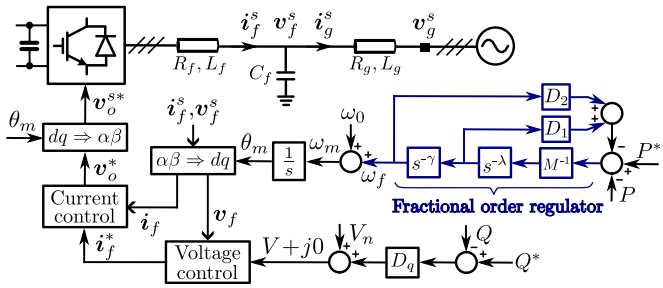

Fig. 1. FOVSG circuit and block diagram.

II. System Description

A test system of an FOVSG connected to the grid is shown in Fig. 1, where the boldface letters denote the vectors. The vectors in the dq frame are written without the superscript s, e.g., the inverter output voltage reference $\boldsymbol{v}_o^*$, and those in the $\alpha\beta$ frame have the superscript s, e.g., $\boldsymbol{v}_o^{s*}$. Regarding the inner cascaded current–voltage regulation, the standard vector control is often applied [11], [12]. Additionally, a fractional-order regulator

Manuscript received 1 December 2022; revised 6 January 2023 and 30 January 2023; accepted 3 February 2023. Date of publication 13 February 2023; date of current version 20 April 2023. This work was supported in part by VILLUM FONDEN under the VILLUM Investigator under Grant 25920, in part by the Ministry of Foreign Affairs of Denmark, in part by Danida Fellowship Centre under Grant 19-M03-AAU, and in part by China Scholarship Council. *(Corresponding author: Yun Yu.)*

The authors are with the Center for Research on Microgrids, AAU Energy, Aalborg University, 9220 Aalborg, Denmark (e-mail: yyu@et.aau.dk; ygu@et.aau.dk; wka@et.aau.dk; skc@et.aau.dk; juq@et.aau.dk; joz@et.aau.dk).

Color versions of one or more figures in this article are available at https://doi.org/10.1109/TPEL.2023.3244670.

Digital Object Identifier 10.1109/TPEL.2023.3244670

and a proportional gain are applied for the active power and reactive power control. Here, the dc-link voltage is assumed to be constant, and its stored energy is taken to be infinite.

III. Theoretical Results

A. FOVSG Basis

In VSG, the inverter is regulated as a voltage source, whose phase angle θ_m and voltage amplitude V are governed by the emulation of synchronous generators (SGs). Disregarding the switching ripple and control latency, the capacitor voltage is expressed in the stationary $\alpha\beta$ frame as $\boldsymbol{v}_f^s = Ve^{j\theta_m}$ where

$$V = D_q\left(Q^* - Q\right) + V_n \tag{1}$$

where V_n denotes the nominal voltage amplitude and D_q is a proportional gain. The active power control law, which is the key of the inertial response emulation, is written as follows:

$$P^* - P = M\frac{d\omega_m}{dt} + D_p\left(\omega_m - \omega_0\right), \quad \frac{d\theta_m}{dt} = \omega_m \tag{2}$$

where ω_0 and ω_m are the fundamental and VSG angular frequencies, respectively; D_p represents the damping constant; and M denotes the ω_0-scaled synthetic inertia, which is written as follows:

$$M = 2HS_{\text{base}}/\omega_0 \tag{3}$$

where H denotes the inertia constant (with dimension time), and S_{base} is the inverter rated apparent power.

According to (2), there are two degrees of freedom, namely M and D_p. This inevitably restricts the flexibility needed to realize satisfactory active power control and inertial response at the same time. The compromise between these two objectives motivates the application of the FOC. Applying the FOC, the active power control law is reconstructed as follows:

$$P^* - P = M\frac{d^{\gamma+\lambda}\omega_f}{dt} + D_1\frac{d^{\gamma}\omega_f}{dt} + D_2\omega_f, \quad \frac{d\theta_m}{dt} = \omega_0 + \omega_f \tag{4}$$

where ω_f is the frequency generated by the fractional operator; D_1 and D_2 are the two feedback gains; and γ and λ are two noninteger numbers. In FOC, the operator order is not necessarily an integer, they can be rational, irrational, or complex numbers, whereas the derivative and integral actions still exist [14].

B. FOVSG Design and Analysis

In accordance with the articles presented in [11] and [15], the grid-side impedance is assumed to be inductive (i.e., $X_g = \omega_0 L_g \gg R_g$), and the grid voltage $\boldsymbol{v}_g^s$ behind the impedance is stiff (i.e., $\boldsymbol{v}_g^s = V_g e^{j\omega_0 t}$).

For analyzing the FOVSG, namely the closed-loop system from P^* to P, the output active power is first formulated as $P = 1.5VV_g\sin\delta/X_g$, where $\delta = \int(\omega_m - \omega_0)dt$ represents the phase angle between VSG and grid voltages. Approximately, $\sin\delta \approx \delta$. Assuming $VV_g \approx V_n^2$ and writing variables as perturbations about the equilibrium point as $x = x_0 + \Delta x$, $\Delta\delta$ yields

$$\Delta\delta = \frac{\Delta\omega_m}{s} = \frac{X_g}{1.5V_n^2}\Delta P \tag{5}$$

where $s = d/dt$. Substituting (5) into (4), the loop gain is

$$G(s) = \frac{1}{Ms^{\gamma+\lambda} + D_1 s^{\gamma} + D_2}\frac{1.5V_n^2}{sX_g}. \tag{6}$$

Now, the stability and the dynamic response of the closed-loop system $\Delta P/\Delta P^* = G(s)/[1 + G(s)]$ can be evaluated. In order to evaluate the inertial effect, the transfer function from the angular frequency deviation $\Delta\omega_m$ to the load change ΔP is derived as follows [11], [12]:

$$F(s) = \frac{\Delta\omega_m}{\Delta P} = -\frac{1}{Ms^{\gamma+\lambda} + D_1 s^{\gamma} + D_2}. \tag{7}$$

With (6) and (7), the FOVSG can be designed to fulfill the power control and inertial response requirements.

1) The First Step: For the FOVSG design and the real-time implementation, the fractional-order derivative should be first synthesized by a recursive distribution of s-domain zeros and poles [14]. For this, the oustaloup recursive approximation is often applied to generate the oustaloup filter as follows [16]:

$$s^o = K\prod_{k=1}^{N}\frac{s + \omega_k'}{s + \omega_k} \tag{8}$$

where o is the order of the derivative; N is the order of the oustaloup filter; and the filter coefficients K, ω_k', and ω_k are given as follows:

$$K = \omega_h^o, \quad \omega_k' = \omega_l\omega_u^{\frac{2k-1-o}{N}}, \quad \omega_k = \omega_l\omega_u^{\frac{2k-1+o}{N}} \tag{9}$$

where $\omega_u = \sqrt{\omega_h/\omega_l}$; ω_l and ω_h denote the boundaries of the frequency range of interest, i.e., (ω_l, ω_h). Considering the accuracy and complexity, in this letter, N is set to 5, and ω_l and ω_h are 0.1 rad/s and 1000 rad/s, respectively [14].

2) The Second Step: Considering the design simplicity, the control stability, and the preservation of the static droop characteristic, the following conditions should be noted.

i) To ensure there is an integer integration in (6): $\gamma + \lambda = 1$, where $\gamma \in (0, 1)$ and $\lambda \in (0, 1)$.

ii) FOVSG should have the same static droop. From (8), we have $\lim_{s\to 0} s^o \neq 0$. Thus, γ, λ, D_1, and D_2 determine $\lim_{s\to 0} F(s)$, simultaneously, and it should be $-D_p^{-1}$.

3) The Third Step: Following the conditions, the number of parameters to be selected will reduce by half, and they can be subsequently tuned via evaluating (6) and (7). For this, three criteria are defined as follows.

a) For a stable FOVSG, all the feedback should be negative, i.e., $D_1 > 0$ and $D_2 > 0$.

b) Phase margin φ_M and crossover frequency ω_{cg}, which are derived from (6), serve as the main measures of the feedback control, whose thresholds are set to 30° and 18 rad/s [17].

c) The cutoff frequency ω_c of $F(s)$ in (7) shows the extent of the inertial effect. To have a strong inertial effect, ω_c should be as small as possible [11], [12].

The VSG data is in Table I. The inertia constant H is set to 2.5 s for a moderate synthetic inertia (in general, 0–5 s), and the damping constant D_p is set to 20 p.u. for a 5% frequency droop. Following the conditions i) and ii), varying γ within $(0, 1)$, and

TABLE I
VSG DATA

Symbol	Value	Symbol	Value	Symbol	Value
S_{base}	2.2 kVA	V_n	$\sqrt{2/3}\cdot 220$ V	ω_0	314 rad/s
X_g	0.083 p.u.	H	2.5 s	D_p	20 p.u.

Note: Base value of D_p is ω_0/S_{base}.

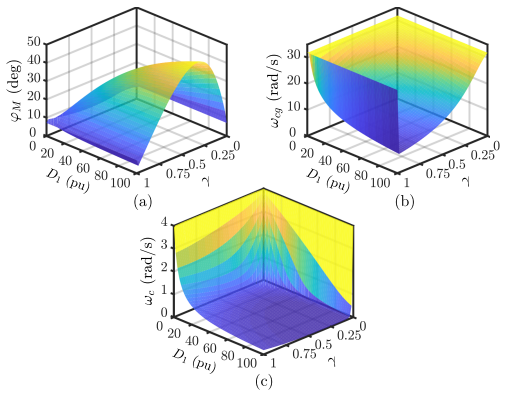

Fig. 2. Main measures of FOVSG. (a) Phase margin φ_M. (b) Crossover frequency ω_{cg}. (c) Cutoff frequency ω_c.

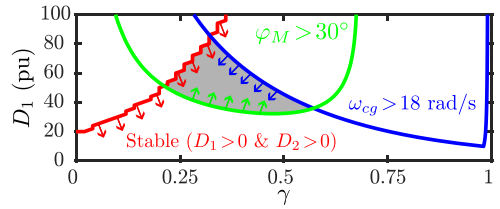

Fig. 3. Feasible parameter range.

varying D_1 within $(0, 100)$ p.u., φ_M, ω_{cg}, and ω_c are obtained, as shown in Fig. 2. Clearly, φ_M varies oppositely as ω_{cg}, which is to be expected as increasing the phase margin often leads to an enhancement of the robustness and a slow dynamic response. Notably, the cutoff frequency ω_c decreases on the entire γ-D_1 plane, which indicates a better inertial effect.

For the selection of γ and D_1, the feasible parameter range is first derived from the criteria a) and b), as shown in Fig. 3. Then, since criterion c) is already met on the entire γ-D_1 plane, γ and D_1 are selected within the gray region. For example, γ is set to 0.43, and D_1 is set to 52 p.u. Subsequently, λ and D_2 are calculated according to conditions i) and ii), and their values are 0.57 and 12.8 p.u.

Substituting γ, λ, D_1, and D_2 into (6) and (7), comparative analyses in the grid-tied and islanded cases are applied, and the corresponding results are shown in Figs. 4 and 5, respectively. In accordance with the articles presented in [11], [12], and [13], the pole–zero map and the step response of $\Delta P/\Delta P^* = G(s)/[1 + G(s)]$ are used for assessing the active power control in the grid-tied case, and the frequency response and the step response of $\Delta\omega_m/\Delta P = F(s)$ are used to assess the frequency dynamic in the islanded case.

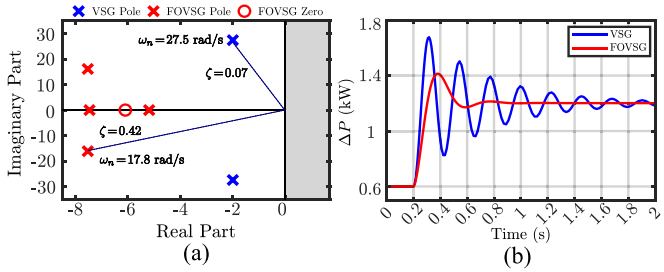

Fig. 4. Analytical results of $\Delta P/\Delta P^* = G(s)/[1 + G(s)]$. (a) Pole–zero map. (b) Step response under a set point step change $\Delta P^* = 0.6$ kW.

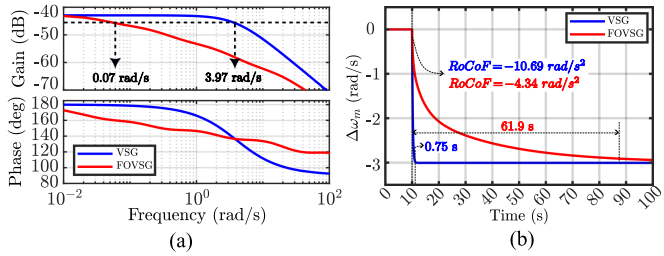

Fig. 5. Analytical results of $\Delta\omega_m/\Delta P = F(s)$. (a) Frequency response. (b) Step response under a load step change $\Delta P = 0.42$ kW.

As depicted in Fig. 4(a), in the case of using VSG, i.e., (2), the damping ratio ζ of the complex poles is around 0.07, and the oscillation frequency ω_n is 27.5 rad/s. In the case of using FOVSG, i.e., (4), extra poles and zeros are introduced, and ζ and ω_n of the dominant complex poles are 0.42 and 17.8 rad/s, respectively. As shown in Fig. 4(b), the step response comparisons under a set point change $\Delta P^* = 0.6$ kW validate the damping effect improvement made by the FOVSG as well.

For the inertial effect evaluation, the transient time of the frequency trajectory is defined as the time it takes to reach 95% of the steady-state frequency, and the RoCoF is [11]

$$\text{RoCoF} = \Delta\omega_{m-3\text{cycle}}/T_{3\text{cycle}} \tag{10}$$

where $\Delta\omega_{m-3\text{cycle}}$ represents the angular frequency deviation after three fundamental periods $T_{3\text{cycle}}$.

Then, $\Delta\omega_m/\Delta P$ is used to evaluate the frequency dynamic under a load change $\Delta P = 0.42$ kW. As shown in Fig. 5(a), the FOVSGs cutoff frequency ω_c reduces from 3.97 to 0.07 rad/s. Correspondingly, in Fig. 5(b), the RoCoF is limited from -10.69 to -4.34 rad/s^2, and the transient time of the frequency trajectory is extended from 0.75 to 61.9 s.

C. Compatibility With the SG

To validate the compatibility with the conventional SG, the power–frequency dynamic of a two-area system model, as shown in Fig. 6(a), is investigated. Based on this model, the simplified block diagram in per-unit form is derived in accordance with the articles presented in [18] and [19], and it is presented in Fig. 6(b). ΔP_1^* and ΔP_2^* are the FOVSG and SG power set point variations. $\Delta\omega_m$ and $\Delta\omega_G$ denote their angular frequency perturbations. In addition, ΔP_{L1} and ΔP_{L2} represent

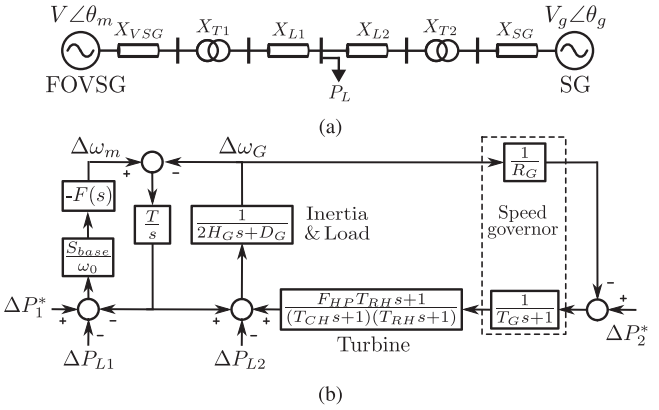

Fig. 6. Two-area system. (a) Equivalent electrical diagram. (b) Block diagram.

TABLE II
TWO-AREA SYSTEM DATA

Areas	Variable	Symbol	Value
Area I FOVSG	Rated power	S_{base}	2.2 kVA
	Inertia constant	H	2.5 s
	Non-integer number	γ	0.43
	Non-integer number	λ	0.57
	Feedback gain	D_1	52 p.u.
	Feedback gain	D_2	12.8 p.u.
	Line inductance	X_1	0.041 p.u.
Area II SG	Rated power	S_{SG}	1 MVA
	Inertia constant	H_G	5 s
	Damping coefficient	D_G	1 p.u.
	Droop constant	R_G	0.05 p.u.
	Speed governor coefficient	T_G	0.1 s
	Turbine HP coefficient	F_{HP}	0.3
	Time constant of reheater	T_{RH}	7 s
	Time constant of main inlet volumes	T_{CH}	0.2 s
	Line inductance	X_2	0.041 p.u.

the load powers fed by two areas, and they can be approximately formulated as [19]

$$\Delta P_{L1} = \frac{X_2}{X_1 + X_2}\Delta P_L, \quad \Delta P_{L2} = \frac{X_1}{X_1 + X_2}\Delta P_L \tag{11}$$

where $X_1 = X_{\text{VSG}} + X_{T1} + X_{L1}$ and $X_2 = X_{\text{SG}} + X_{T2} + X_{L2}$. ΔP_L is the total load power perturbation.

Moreover, in Fig. 6(b), H_G is the SG inertia constant, and D_G is the load damping coefficient. R_G and T_G denote the droop factor and time constant of the speed governor, respectively. F_{HP}, T_{RH}, and T_{CH} denote the reheat turbine coefficients [18]. Additionally, the synchronization torque coefficient T is set to $1.5V_n^2\omega_0/[S_{\text{base}}(X_1+X_2)]$. Subsequently, the closed-loop system $\Delta\omega_m/\Delta P_L$ is used to verify the frequency dynamic under a load change. Using the data presented in Table II, the frequency response of $\Delta\omega_m/\Delta P_L$ and the system frequency trajectory under a 0.1 p.u. load change are depicted in Fig. 7(a) and (b), respectively.

It is clear that the cutoff frequency of $\Delta\omega_m/\Delta P_L$ reduces remarkably from 3.86 to 0.5 rad/s when the proposed FOVSG is applied to replace the VSG. Correspondingly, the RoCoF and the frequency nadir are significantly limited, which validates the

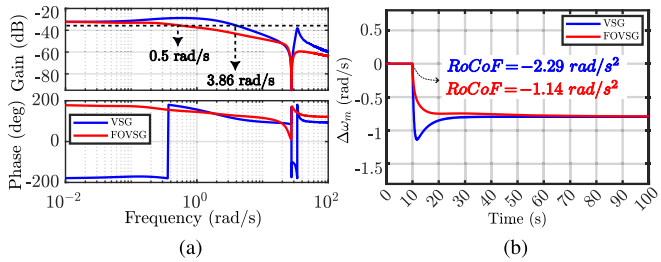

Fig. 7. Analytical results of $\Delta\omega_m/\Delta P_L$. (a) Frequency response. (b) Step response under a load change of 0.1 p.u.

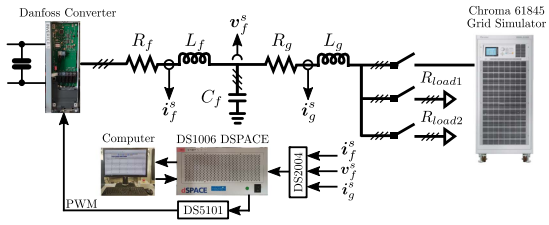

Fig. 8. Experimental setup.

TABLE III
EXPERIMENTAL SETUP DATA

Variable	Symbol	Value
Rated power	S_{base}	2.2 kVA
Nominal voltage	V_n	$\sqrt{2/3}\cdot 220$ V
Filter resistance	R_f	0.1 Ω
Filter inductance	L_f	1.8 mH
Filter capacitance	C_f	9 μF
Grid resistance	R_g	0.5 Ω
Grid inductance	L_g	5.5 mH
Fundamental frequency	ω_0	314 rad/s
Switching frequency	f_{sw}	10 kHz
Resistive loads	$R_{\text{load1,2}}$	115 Ω

compatibility with the SG and the inertial effect improvement introduced by the FOVSG.

IV. EXPERIMENTAL VALIDATIONS

The experimental validation is conducted using a laboratory implementation in [11], [12], and [13], as shown in Fig. 8. VSG and FOVSG control parameters are given in Table I and Table II, respectively. The setup data are given in Table III. The control is realized via the DSPACE DS1006 processor. With respect to the digital realization, the Tustin discretization method is applied in this letter for both VSG and FOVSG [14]. Using (2), (4), (8), and (9), the discretization can be automatically realized in MATLAB, and the resulting regulators are 2nd and 11th order ($N\times 2+1$), respectively. The computational burden in both cases is negligible for digital processors.

The results in the grid-tied case with set point step changes of 0.6 kW and the islanded case with load changes of 0.42 kW are recorded by an oscilloscope and shown in Figs. 9–11. Then, we have the following observations.

1) In the grid-tied case, as shown in Fig. 9, under a set point step change, obvious power oscillations can be observed

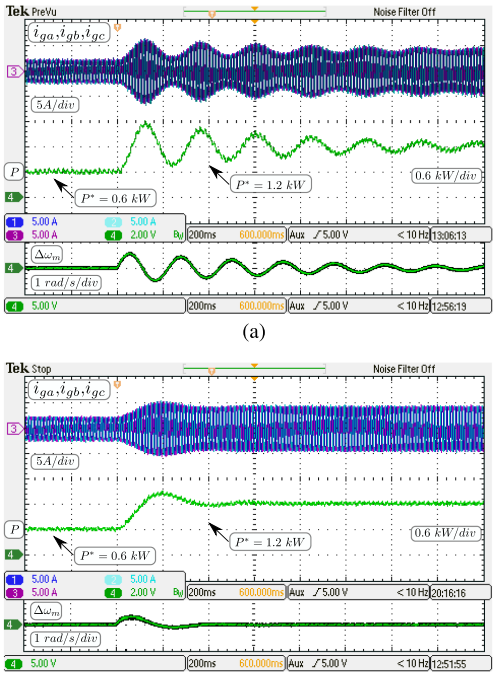

Fig. 9. Current, active power, and angular frequency in the grid-tied case. (a) VSG. (b) FOVSG.

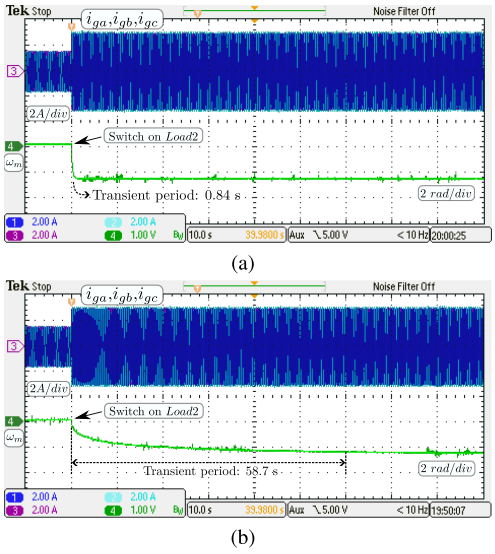

Fig. 10. Current and angular frequency in the islanded case. (a) VSG. (b) FOVSG.

in the VSG, whereas the FOVSG can effectively mitigate the oscillations without degrading the tracking accuracy.

2) In the islanded case, the inverter first supplies a resistive load R_{load1}. When a load variation is suddenly applied, i.e., switching on R_{load2}, frequency drops quickly when the conventional VSG is applied, as shown in Fig. 10(a). In comparison, with the same inertia constant and static droop, the FOVSG extends the transient time of the frequency trajectory from 0.84 to 58.7 s, as depicted in Fig. 10(b), which indicates a significant inertial response improvement. A zoom of the frequency transient is shown in Fig. 11. From (10), the RoCoFs are -9.87 and -4.03 rad/s^2, and the improvement over the conventional VSG is $(9.87-4.03)/9.87\times 100\% = 59.2\%$.

3) The oscillation frequency (26.17 rad/s), the transient time of the frequency trajectory (0.84 and 58.7 s), and the RoCoF (-9.87 and -4.03 rad/s^2) are close to the analytical results, as shown in Figs. 4 and 5, which validates the theoretical analyses applied in this letter.

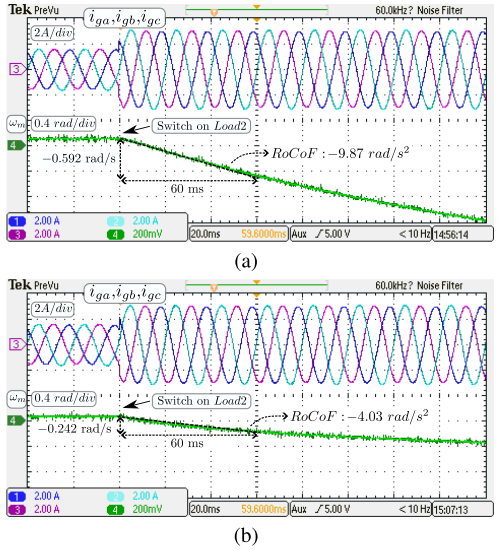

Fig. 11. Initial RoCoF. (a) VSG. (b) FOVSG.

V. Conclusion

In this letter, the FOC is used to improve the conventional VSG, and a novel FOVSG scheme is presented. The stability and improved performance of FOVSG are proven theoretically, and they are demonstrated through experimental verification in the laboratory. Compared with the VSG, the FOVSG provides enhanced damping of the power oscillations in the grid-tied case. Furthermore, in the islanded case, the FOVSG provides a better inertial effect for slowing down the frequency dynamics. Specifically, the initial RoCoF has been improved by 59.2% over the VSG. It is noteworthy that the FOVSG is developed using the assumption that the dc link is ideal; however, the energy storage of the dc link has its own limitation. Then, the energy storage requirement of the FOVSG needs to be further investigated, where the dc-link dynamic and its regulation should be considered. Moreover, applying the FOVSG scheme, the synchronization and the overcurrent prevention under fault conditions can be included in the further research.

References

[1] J. Liu, Y. Miura, and T. Ise, "Comparison of dynamic characteristics between virtual synchronous generator and droop control in inverter-based distributed generators," *IEEE Trans. Power Electron.*, vol. 31, no. 5, pp. 3600–3611, May 2016.

[2] T. Shintai, Y. Miura, and T. Ise, "Oscillation damping of a distributed generator using a virtual synchronous generator," *IEEE Trans. Power Del.*, vol. 29, no. 2, pp. 668–676, Apr. 2014.

[3] L. Huang, H. Xin, and Z. Wang, "Damping low-frequency oscillations through VSC-HVDC stations operated as virtual synchronous machines," *IEEE Trans. Power Electron.*, vol. 34, no. 6, pp. 5803–5818, Jun. 2019.

[4] S. Dong and Y. C. Chen, "Adjusting synchronverter dynamic response speed via damping correction loop," *IEEE Trans. Energy Convers.*, vol. 32, no. 2, pp. 608–619, Jun. 2017.

[5] P. Sun, J. Yao, Y. Zhao, X. Fang, and J. Cao, "Stability assessment and damping optimization control of multiple grid-connected virtual synchronous generators," *IEEE Trans. Energy Convers.*, vol. 36, no. 4, pp. 3555–3567, Dec. 2021.

[6] Z. Shuai, W. Huang, Z. J. Shen, A. Luo, and Z. Tian, "Active power oscillation and suppression techniques between two parallel synchronverters during load fluctuations," *IEEE Trans. Power Electron.*, vol. 35, no. 4, pp. 4127–4142, Apr. 2020.

[7] Y. Yang et al., "A new virtual inductance control method for frequency stabilization of grid-forming virtual synchronous generators," *IEEE Trans. Ind. Electron.*, vol. 70, no. 1, pp. 441–451, Jan. 2023.

[8] J. Liu, Y. Miura, and T. Ise, "Fixed-parameter damping methods of virtual synchronous generator control using state feedback," *IEEE Access*, vol. 7, pp. 99177–99190, 2019.

[9] J. Liu, Y. Miura, and T. Ise, "A comparative study on damping methods of virtual synchronous generator control," in *Proc. 21st Eur. Conf. Power Electron. Appl.*, 2019, pp. 1–10.

[10] Y. Yu et al., "A comparison of fixed-parameter active-power-oscillation damping solutions for virtual synchronous generators," in *Proc. 47th Annu. Conf. IEEE Ind. Electron. Soc.*, 2021, pp. 1–6.

[11] X. Meng, J. Liu, and Z. Liu, "A generalized droop control for grid-supporting inverter based on comparison between traditional droop control and virtual synchronous generator control," *IEEE Trans. Power Electron.*, vol. 34, no. 6, pp. 5416–5438, Jun. 2019.

[12] D. B. Rathnayake, R. Razzaghi, and B. Bahrani, "Generalized virtual synchronous generator control design for renewable power systems," *IEEE Trans. Sustain. Energy*, vol. 13, no. 2, pp. 1021–1036, Apr. 2022.

[13] Y. Yu et al., "A reference-feedforward-based damping method for virtual synchronous generator control," *IEEE Trans. Power Electron.*, vol. 37, no. 7, pp. 7566–7571, Jul. 2022.

[14] C. A. Monje, Y. Chen, B. M. Vinagre, D. Xue, and V. Feliu-Batlle, *Fractional-Order Systems and Controls*, 1st ed. London, U.K.: Springer, 2010.

[15] L. Harnefors, F. M. M. Rahman, M. Hinkkanen, and M. Routimo, "Reference-feedforward power-synchronization control," *IEEE Trans. Power Electron.*, vol. 35, no. 9, pp. 8878–8881, Sep. 2020.

[16] A. Oustaloup, F. Levron, B. Mathieu, and F. M. Nanot, "Frequency-band complex noninteger differentiator: Characterization and synthesis," *IEEE Trans. Circuits Syst. I, Fundam. Theory Appl.*, vol. 47, no. 1, pp. 25–39, Jan. 2000.

[17] G. F. Franklin, J. D. Powell, and A. Emami-Naeini, *Feedback Control of Dynamic Systems*, 4th ed. Upper Saddle River, NJ, USA: Prentice hall, 2002.

[18] J. Fang, H. Li, Y. Tang, and F. Blaabjerg, "Distributed power system virtual inertia implemented by grid-connected power converters," *IEEE Trans. Power Electron.*, vol. 33, no. 10, pp. 8488–8499, Oct. 2018.

[19] A. González-Cajigas, J. Roldán-Pérez, and E. J. Bueno, "Design and analysis of parallel-connected grid-forming virtual synchronous machines for island and grid-connected applications," *IEEE Trans. Power Electron.*, vol. 37, no. 5, pp. 5107–5121, May 2022.